Asian Journal of Pharmaceutical Sciences 18 (2023) 100872

Available online at www.sciencedirect.com

ScienceDirect

journal homepage: www.elsevier.com/locate/AJPS

Research Article

A nanocomposite competent to overcome cascade drug resistance in ovarian cancer *via* mitochondria dysfunction and NO gas synergistic therapy

Min Zhong[a,1], *Peiqin Liang*[a,1], *Zhenzhen Feng*[b,1], *Xin Yang*[a], *Guang Li*[a], *Rui Sun*[c], *Lijuan He*[a], *Jinxiu Tan*[a], *Yangpengcheng Xiao*[a], *Zhiqiang Yu*[b,c,*], *Muhua Yi*[d,*], *Xuefeng Wang*[a,*]

[a] *Department of Obstetrics and Gynecology, The Third Affiliated Hospital of Southern Medical University, Guangzhou 510632, China*
[b] *School of Pharmaceutical Sciences, Guangdong Provincial Key Laboratory of New Drug Screening, Southern Medical University, Guangzhou 510515, China*
[c] *Department of Laboratory Medicine, Dongguan Institute of Clinical Cancer Research, The Tenth Affiliated Hospital of Southern Medical University (Dongguan people's hospital), Dongguan 523018, China*
[d] *Department of Pathology, Affiliated Dongguan Hospital, Southern Medical University, Dongguan 523059, China*

ARTICLE INFO

Article history:
Received 16 May 2023
Revised 20 October 2023
Accepted 26 November 2023
Available online 30 November 2023

Keywords:
Cisplatin resistance
Patient-derived xenograft model
Mitochondrial dysfunction
Nitric oxide
Ovarian cancer

ABSTRACT

Ovarian cancer (OC) is one of the most common and recurring malignancies in gynecology. Patients with relapsed OC always develop "cascade drug resistance" (CDR) under repeated chemotherapy, leading to subsequent failure of chemotherapy. To overcome this challenge, amphiphiles (P1) carrying a nitric oxide (NO) donor (Isosorbide 5-mononitrate, ISMN) and high-density disulfide are synthesized for encapsulating mitochondria-targeted tetravalent platinum prodrug (TPt) to construct a nanocomposite (INP@TPt). Mechanism studies indicated that INP@TPt significantly inhibited drug-resistant cells by increasing cellular uptake and mitochondrial accumulation of platinum, depleting glutathione, and preventing apoptosis escape through generating highly toxic peroxynitrite anion ($ONOO^-$). To better replicate the microenvironmental and histological characteristics of the drug resistant primary tumor, an OC patient-derived tumor xenograft (PDX^{OC}) model in BALB/c nude mice was established. INP@TPt showed the best therapeutic effects in the PDX^{OC} model. The corresponding tumor tissues contained high $ONOO^-$ levels, which were attributed to the simultaneous release of $O_2^{\bullet-}$ and NO in tumor tissues. Taken together, INP@TPt-based systematic strategy showed considerable potential and satisfactory biocompatibility in overcoming platinum CDR, providing practical applications for ovarian therapy.

© 2023 Shenyang Pharmaceutical University. Published by Elsevier B.V.
This is an open access article under the CC BY-NC-ND license
(http://creativecommons.org/licenses/by-nc-nd/4.0/)

* Corresponding authors.
E-mail addresses: yuzq@smu.edu.cn (Z. Yu), yimuhuaaini@126.com (M. Yi), douwangxuefeng@163.com (X. Wang).
[1] These authors contributed equally to this work.
Peer review under responsibility of Shenyang Pharmaceutical University.

https://doi.org/10.1016/j.ajps.2023.100872
1818-0876/© 2023 Shenyang Pharmaceutical University. Published by Elsevier B.V. This is an open access article under the CC BY-NC-ND license (http://creativecommons.org/licenses/by-nc-nd/4.0/)

1. Introduction

Ovarian cancer (OC) is one of the most common malignancies in gynecology, with the highest mortality rate [1]. In three European studies consisting of 1620 patients with OC, median progression free survival and overall survival was 10.2 [95% confidence interval (CI): 9.6–10.7] and 17.6 (95% CI: 16.4–18.6) months, respectively [2]. At present, the primary treatment option for OC is standard surgery combining with platinum-based chemotherapy [3]. Cisplatin (cis-diaminedichlorop, CDDP), a representative platinum-based drug, is widely used in the chemotherapy treatment of OC. However, many patients with repeated chemotherapy due to multiple relapses, show platinum resistance [4–6]. The cisplatin resistance may result from multiple mechanisms, including reduced accumulation of intracellular cisplatin, increased detoxification by glutathione (GSH), the tumor cell DNA damage repair, and processes that lead to tumor cell apoptosis escape [7]. Taken together, these resistance mechanisms are defined as "cascade drug resistance'' (CDR) [8]. Considering the high relationship between cisplatin resistance and poor prognosis, it is important to develop more effective therapeutic strategies, which target all processes involved in the CDR of cisplatin.

The cisplatin-resistant cell is characterized as the abnormal level of Copper Transporter 1 (CTR1) and GSH. CTR1 plays an important role in actively transporting cisplatin inside of cells, however, accelerated degradation, reduced expression and unique glycosylation have been found in cisplatin-resistant ovarian cancer cells [9,10]. Nanoparticle-based drug delivery systems (NDDSs) have been successfully used to bypass the need of active transport by CTR1 through cellular uptake [11–13]. GSH is the principal intracellular sulfhydryl-containing substance that detoxifies cisplatin in cisplatin-resistant cells [14,15]. Current studies have also shown that NDDS containing disulfide or diselenium bonds can deplete intracellular GSH and prevent cisplatin from being detoxified [16,17]. Furthermore, cisplatin needs to induce DNA cross-linking to achieve anticancer effects, however, the DNA repairing effect of the nucleus is responsible for prohibiting the effect of cisplatin in resistant cells [18–20]. Mitochondria, which are enriched in mitochondrial DNA but lack powerful DNA repairing ability, are considered a potential target for cisplatin [21–26]. When disrupted by cisplatin, superoxide ($O_2^{\bullet-}$) and ATP are released from the mitochondrial respiratory chain, thus promoting apoptosis of tumor cells [23,27-34]. Therefore, mitochondria could be ideal target organelles for overcoming cascade drug resistance.

Reactive nitrogen species (RNS) including peroxynitrite anion ($ONOO^-$), nitrate anion (NO^-), nitrite ion (NO_2^-) and etc. are essential free radical reactive substances with strong oxidizing and nitrifying abilities [35–38]. RNS can lead to cell apoptosis *via* peroxidation and nitrification of biomolecules [37,39-41]. Among the various kinds of RNS, $ONOO^-$ is the most lethal one because of its stronger peroxide capacity [42,43]. Notably, the reaction of nitric oxide (NO) and reactive oxygen species (ROS), such as $O_2^{\bullet-}$, can generate $ONOO^-$ [44–46]. The logical integrated advantages of cisplatin and RNS therefore prompted us to construct a mitochondria specific treatment strategy against CDR.

Here, a systematic strategy was proposed by constructing nanocomposite INP@TPt, which was self-assembled from amphiphiles (P1) and mitochondria-targeted tetravalent platinum prodrug (TPt) (Scheme 1A). The P1 was consisting of a NO donor (isosorbide 5-mononitrate, ISMN) and disulfide bond. To replicate the microenvironmental and histological characteristics of the primary tumor, an ovarian cancer patient-derived tumor xenograft (PDX^{OC}) model was established in BALB/c nude mice (Scheme 1B). INP@TPt was able to overcome cisplatin CDR by targeting at least four resistance mechanisms (Scheme 1C): (1) INP@TPt increased cellular uptake of platinum by enhanced permeability and retention (EPR) effects to deliver tetravalent platinum prodrugs; (2) INP@TPt reduced platinum detoxification by depleting intracellular GSH; (3) INP@TPt elevated the levels of platinum in the mitochondria by releasing TPt, and (4) INP@TPt decreased apoptosis escape of cisplatin-resistance cells by generating RNS. *In vitro* and *in vivo* results indicated that INP@TPt overcome cisplatin CDR in OC cells and inhibited tumor growth in the PDX^{OC} model.

2. Materials and methods

2.1. Materials

Cisplatin was purchased from InvivoChem (Libertyville, USA). Succinic anhydride, dodecyl isocyanate, (2-aminoethyl) triphenylphosphonium bromide, 2,2-Disulfanediylbis(ethan-1-ol) (DSB), (1,2,4,5-Cyclohexanetertracarboxylicdianhydrid (CHTA), Isosorbide 5-mononitrate (ISMN), rhodamine B (tetraethyl rhodamine), and 3-(4,5- dimethyl-2-thiazolyl)-2,5-diphenyl-2-H-tetrazolium bromide (MTT) were purchased from TCI, Aladdin (China), and mPEG5000 was purchased from AVT Pharmaceutical Tech Co., Ltd. (Shanghai, China). Cell culture dishes, cell cultured 6-well plates, 96-well plates were purchased from NEST Biotechnology (Wuxi, China). NO fluorescence probe, Reactive Oxygen Species Assay Kit, Mitochondrial Membrane Potential Assay Kit were purchased from Beyotime (Shanghai, China), RNS fluorescence probe was purchased from BestBio (Nanjing, China). Annexin V-FITC apoptosis detection kit was purchased from YEASEN Biotechnology (Shanghai China). Glutathione (GSH) kit, ATP detection kit Mitochondrial extraction kit and Nucleus extraction kit was purchased from Solarbio Science & Technology Co., Ltd. (Beijing, China). Rabbit Anti-rat IgM/Bio antibody was purchased from Jiangsu Jingmei Biotechnology Co, Ltd (Yancheng, China). The other antibodies were bought from Abcam. RPMI 1640 medium and fetal bovine serum (FBS) were purchased from Inner Mongolia Opcel Biotechnology Co., Ltd (Huhhot, China).

2.2. Preparation of INP@Pt(IV), NP@TPt and INP@TPt

P1 (8 mg) and Pt(IV) (2 mg) were fully dissolved in 1 ml DMSO. Then the solution was added to 1 ml water dropwise under the

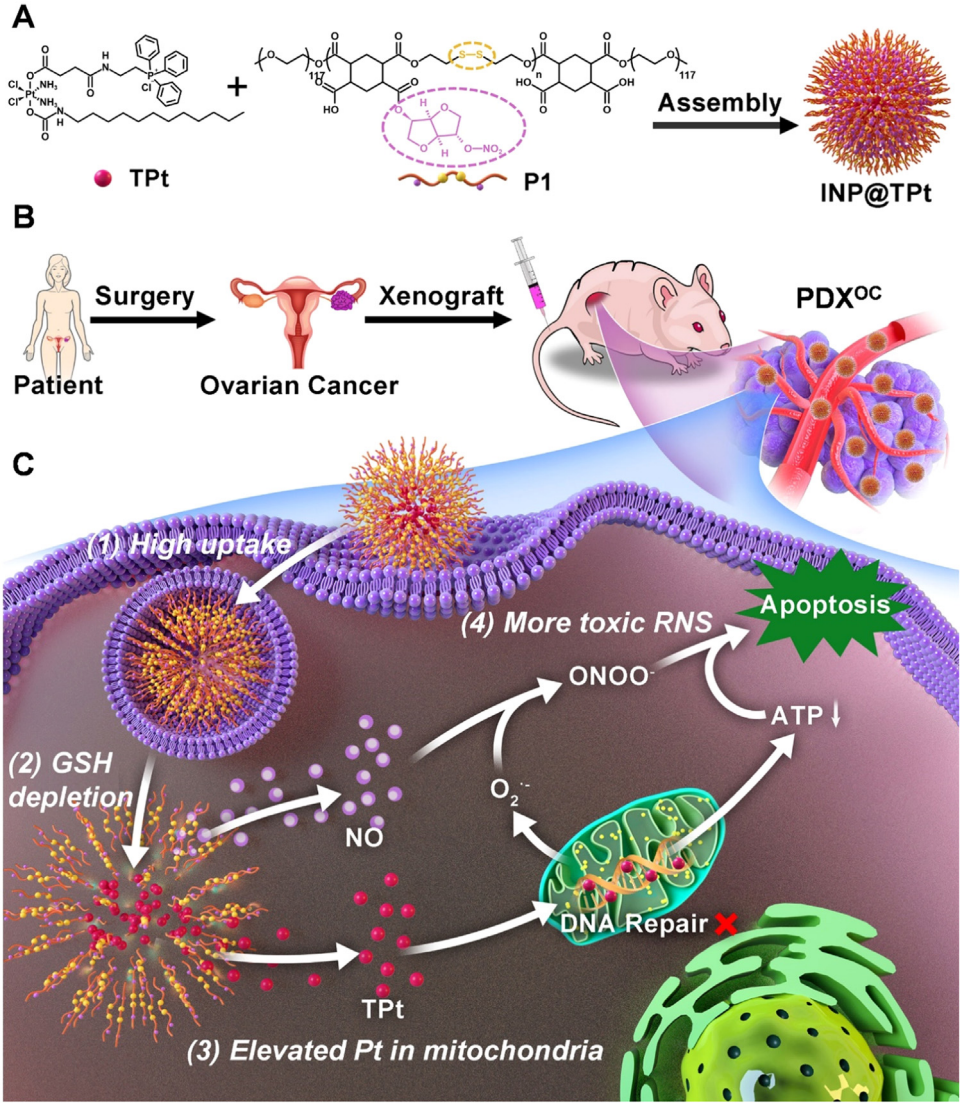

Scheme 1 – Schematic illustration of the nanoparticle (INP@TPt) for overcoming cisplatin "cascade drug resistance" in ovarian cancer. (A) Synthesis of INP@TPt. (B) The establishment of the PDX^{OC} model. (C) Antitumor mechanisms of INP@TPt: (1) increased cellular uptake of platinum, (2) reduced the detoxification of platinum by depleting GSH and release of TPt as well as NO after fracture of GSH-responsive polymer, (3) increased accumulation of platinum in the mitochondrial, thereby inducing mitochondrial dysfunction and releasing $O_2^{\cdot -}$ from the mitochondria and reducing ATP production, and (4) preventing apoptosis escape by producing highly toxic $ONOO^-$.

ultrasonic wave. The nanoparticles were purified by dialysis (MWCO: 3500 Da). The product was named INP@Pt(IV). NP@TPt and INP@TPt were obtained with the same method.

2.3. *GSH consumption of P1 and P2*

P1 (1.5 mg) and P2 (1.5 mg) were added separately to 15 μl dimethyl formamide. Equal volumes of phosphate-buffered saline (PBS), P1 and P2 were then added separately to 10 mM GSH, and the concentration of GSH was measured after 1 h using a commercially available GSH kit (Solarbio, China).

2.4. *Cell lines and animals*

A2780 (human ovarian cancer cell line) and A2780DDP (human cisplatin-resistant ovarian cell line), sourced from the cell repository at the School of Pharmaceutical Sciences, Southern Medical University, were cultured in complete RPMI-1640 containing 10% FBS and 1% penicillin–streptomycin. Female BALB/c nude mice aged 4–6 weeks were purchased from Guangdong Medical Laboratory Animal Center (Guangdong, China). All animal experiments were conducted in accordance with the guidelines evaluated and approved by the Zhujiang Hospital Ethics Committee of Southern Medical University

(LAEC-2020–093). The patient-derived tumor xenograft model derived from human ovarian cancer tissues received formal ethical approval from the Medical Ethics Committee of Tongji Medical College, Huazhong University of Science and Technology (Approval: 2020S357).

2.5. Cell viability assays

A2780/A2780DDP cells (5×10^3 per well) were cultured in 96-well plates overnight and treated with different formulations [CDDP, Pt(IV), TPt, INP@Pt(IV), NP@TPt and INP@TPt)] at the same concentrations ranging (from 0.3125 to 40 μM). The cells were then maintained for another 48 h and monitored using a MTT assay (Aladdin, China).

2.6. Cell apoptosis assays

After being seeded into a 6-well plate (5×10^5 cells/well) overnight for incubation, A2780DDP cells were treated with PBS, CDDP, Pt(IV), TPt, INP@Pt(IV), NP@TPt or INP@TPt (3 μM Pt) for 48 h. A cell apoptosis assay used the Annexin V-FITC/PI apoptosis detection kit (YEASEN, China) according to the manufacturer's procedure through flow cytometry (FCM) (BD FACSCanto II, U.S.A).

2.7. Intracellular GSH level

A2780DDP cells were seeded in 6-well plates (1×10^6) and treated with PBS, CDDP, NP@TPt or INP@TPt (4 μM Pt) and cultured for 6 h. The cells were then collected and the GSH level was measured using a GSH kit following the manufacturer's procedure (Solarbio, China).

2.8. Nuclear and mitochondrial distribution of Pt

A2780DDP cells were seeded in a petri dish (2×10^6) and cultured overnight, followed by incubation with CDDP, Pt(IV), TPt, INP@Pt(IV) or INP@TPt (10 μM Pt) for 4 h. Mitochondria in the cells (1×10^6) were then extracted using a mitochondrial extraction kit (Solarbio, China). The nuclei from equal numbers of cells (1×10^6) were extracted using a cell nuclei extraction kit (Solarbio, China). The Pt contents of nuclear and mitochondrial extracts were measured using inductively-coupled plasma mass spectrometry (ICP-MS).

2.9. ATP content analysis

A2780DDP cells were seeded in 6-well plates (5×10^5) and cultured overnight, followed by incubation with PBS, CDDP, Pt(IV), TPt, INP@Pt(IV), NP@TPt, or INP@TPt (3 μM Pt) for 48 h. A2780DDP cells were then collected, and the ATP content was determined using an ATP detection kit according to the manufacturer's procedure (Solarbio, China).

2.10. Mitochondrial membrane potential (MMP) depolarizes

A2780DDP cells were seeded in 6-well plates (5×10^5) and cultured overnight, followed by incubation with PBS, CDDP, Pt(IV), TPt, INP@Pt(IV), NP@TPt, or INP@TPt (3 μM Pt) for 48 h. A2780DDP cells were then collected, and MMPs were detected using an MMP assay kit following the manufacturer's procedure for analysis by FCM (Beyotime, China).

2.11. Intracellular NO generation

A2780DDP cells were seeded in 6-well plates (5×10^5) and cultured overnight, followed by incubation with PBS, Pt(IV), TPt, INP@Pt(IV), or INP@TPt (3 μM Pt) for 6 h. All cells were stained with 4-Amino-5-Methylamino-2′,7′-Difluorofluorescein Diacetate (DAM-FM DA) and incubated for 30 min, then washed with PBS, followed by Confocal laser scanning microscope (CLSM) observations or FCM measurements.

2.12. Intracellular ROS generation

A2780DDP cells were seeded in 6-well plates (5×10^5) and cultured overnight, followed by incubation with PBS, CDDP, Pt(IV), TPt, INP@Pt(IV), NP@TPt or INP@TPt (1 μM Pt) for 48 h. All cells were stained with 2′,7′-dichlorofluorescin diac-etate (DCFH-FM DA) and incubated for 30 min, then washed with PBS, followed by FCM measurements.

2.13. Intracellular RNS generation

A2780DDP cells were seeded in 6-well plates (5×10^5) and cultured overnight, followed by incubation with PBS, Pt(IV), TPt, INP@Pt(IV), or INP@TPt (3 μM Pt) for 48 h. All cells were stained with O52 and incubated for 30 min, then washed with PBS, followed by CLSM observations or FCM measurements (BestBio, China).

2.14. Western blotting

A2780DDP cells were seeded in 6-well plates (1×10^6) and cultured overnight, followed by incubation with PBS, CDDP, Pt(IV), TPt, INP@Pt(IV), NP@TPt, or INP@TPt (3 μM Pt) for 48 h. All cells were collected to extract protein, which was equally resolved using SDS-PAGE gels and analyzed by 12% denaturing polyacrylamide gels. Vital proteins, including γ-H2A.X, Bcl-2, Caspase-3, C-Caspase-3, PARP, C-PARP, and β-actin, were then detected.

2.15. In vivo imaging

Cy5.5-loaded P1 nanoparticles (INP@Cy5.5) were prepared. PDX^{OC} model BALB/c nude mice were then injected with INP@Cy5.5. The fluorescence images of mice at 0, 4, 8, 12, 24 and 48 h after injection were performed with an IVIS Lumina III imaging system. After the mice were sacrificed, tumors, as well as major organs, were collected for *ex vivo* imaging at 24 h postinjection.

2.16. In vivo distribution of Pt

PDX^{OC} model BALB/c nude mice were injected intravenously with CDDP and INP@TPt (1.5 mg/kg Pt). After 24 h, tumors and major organs were isolated and nitrated to analyze Pt content using ICP-MS.

2.17. GSH content in the PDX^{OC} tumor

The tumors of PDX^{OC}-bearing mice treated with PBS or INP@TPt for 24 h were isolated and pulverized for the measurement of GSH according to the manufacturer's procedure

2.18. $ONOO^-$ generation in the PDX^{OC} tumor

PDX^{OC} model BALB/c nude mice were injected intravenously with PBS and INP@TPt. After 48 h, the mice received another injection. After 72 h, the mice were sacrificed, and tumors were isolated and stained with O58 according to the manufacturer's procedure (BestBio, China).

2.19. Statistical analysis

Data are represented as the mean ± standard deviation. One-way analysis of variance was used for statistical significance as $^*P < 0.05$; $^{**}P < 0.01$; and $^{***}P < 0.001$.

3. Results and discussion

3.1. Preparation and characterization of nanoparticles

The tetravalent cisplatin with or without mitochondria targeting function [TPt and Pt(IV)] was synthesized (Fig. S1-S4). The amphiphilic polymer with or without NO donors (P1 and P2) was procured by condensation polymerization (Fig. S5-S9). The molecular weights (Mn) of P1 and P2, as determined by gel permeation chromatography (GPC) (Table S2), were 27,830 Da and 28,029 Da, respectively. The nanoprecipitation method was used to synthesize the TPt-encapsulated P1 micellar nanoparticles (INP@TPt) (Fig. 1A), whose loading content of TPt was calculated as 6.8% (wt) using ICP-MS. The scanning electron microscopy (SEM) images revealed that INP@TPt was spherical with a diameter of 106.69 ± 15.26 nm (Fig. 1B). The hydrated size and zeta potential of INP@TPt was measured as 168.72 ± 14.93 nm and −27.83 ± 0.69 mV, respectively (Fig. 1C and S10). There were no drastic size and polydispersity index (PDI) changes of INP@TPt upon incubating with 10% FBS or PBS for 7 d (Fig. 1D), indicating its good stability in the circulation. The high angle annular darkfield scanning transmission electron microscopy (HAADF-STEM) and corresponding energy-dispersive X-ray spectroscopy (EDS) mapping images showed that S, Pt, Cl and N elements were uniformly distributed in the INP@TPt nanoparticle (Fig. 1E). The amphiphilic polymers (P1 and P2) were tailored to consume intracellular GSH through a substantial number of disulfide bonds, while only P1 could produce NO through its own carried organic nitrogen. In the X-ray photoelectron spectroscopy (XPS) analysis of P1 (Fig. 1F), binding energies of 163.28 and 164.58 eV corresponded to the S2p3/2 and S2p1/2, respectively, which were substantially reduced upon incubation with 10 mM GSH. The GSH levels (1 mM) were reduced to 43.43% and 78.41% after reaction with 0.1 mM P1 and P2, respectively, for 1 h (Fig. 1G), because the disulfide bonds contained in P1 and P2 consumed GSH. *In vitro* Pt release profiles of INP@TPt showed that there was a difference in the cumulative Pt release in 10 mM GSH solutions, when compared to PBS. The cumulative Pt release was 80.6% in 10 mM GSH; however, the cumulative release was less than 12.0% in PBS (Fig. 1H). Nanocomposites of NP@TPt assembled from TPt and P2 were also used to evaluate Pt release. Fig. S11 shows that the cumulative Pt release results for INP@TPt and NP@TPt were essentially similar, indicating that the micellar nanoparticles consisting of P1 and P2 had appreciable responsiveness to GSH, making it an ideal drug carrier to achieve precise cytotoxicity while reducing systemic side effects. The above results confirmed the successful synthesis of INP@TPt together with its GSH depletion and Pt release abilities.

3.2. The endocytosis and cytotoxicity of INP@TPt

Based on the above results, the therapeutic effect of INP@TPt on Pt-sensitive (A2780) and Pt-resistant (A2780DDP) ovarian cancer cells were evaluated. To increase drug internalization, INP@TPt circumvented the conventional cisplatin uptake pathway (CTR1) *via* nanocarrier delivery [47]. P1 was labeled with rhodamine B (INP@Rh B) to visualize and quantify the uptake of INP@TPt. CLSM and FCM showed that the fluorescence signal of Rh B in the cells increased with incubation time, indicating a time-dependent effective internalization of INP@Rh B in A2780DDP cells (Fig. 2A&2B and S12&S13). Fig. S14 showed that cellular uptake of INP@TPt was significantly reduced at 4 °C, indicating its energy-dependent nature. Moreover, treatment with chlorpromazine (CPZ) resulted in a substantial decrease in internalization, suggesting that clathrin-mediated endocytosis served as the primary uptake pathway for INP@TPt in A2780DDP cells. ICP-MS results showed that Pt accumulation in INP@TPt increased approximately 12.3-fold, when compared to CDDP alone (Fig. 2C). Furthermore, the cytotoxicities of INP@TPt were assessed in A2780 and A2780DDP cells (Fig. 2D-2E and Table S1), which showed that the IC_{50} of CDDP in A2780 cells was significantly lower than that in A2780DDP cells (IC_{50} A2780 = 2.03 ± 0.13 μM *vs* IC_{50} A2780DDP = 15.29 ± 0.77 μM), denoting >7.53-fold drug resistance. INP@TPt improved the anticancer effect on A2780DDP cells (IC_{50} = 1.33 ± 0.10 μM Pt), which was almost more than eleven-fold higher than CDDP. This result showed that INP@TPt can significantly alleviated CDDP resistance in A2780DDP cells. Then, FCM was used to evaluate the apoptosis of A2780DDP cells after treatment with different groups, INP@Pt(IV) assembled from Pt(IV) and P1 served as a control group without mitochondria targeting ability. Fig. 2F showed significantly increased apoptosis in INP@TPt-treated cells (81.39% ± 3.96%), when compared to the CDDP, INP@Pt(IV) and NP@TPt groups (15.04% ± 2.42%, 53.72% ± 1.67% and 69.28% ± 3.07%). These results indicated that INP@TPt enhanced the cytotoxicity towards CDDP-resistant cancer cells.

3.3. GSH depletion and mitochondrial dysfunction

The remarkable effects of INP@TPt motivated us to further explore the antitumor mechanism within A2780DDP cells. The GSH level of A2780DDP cells after reaction with different groups was detected, which showed a significant

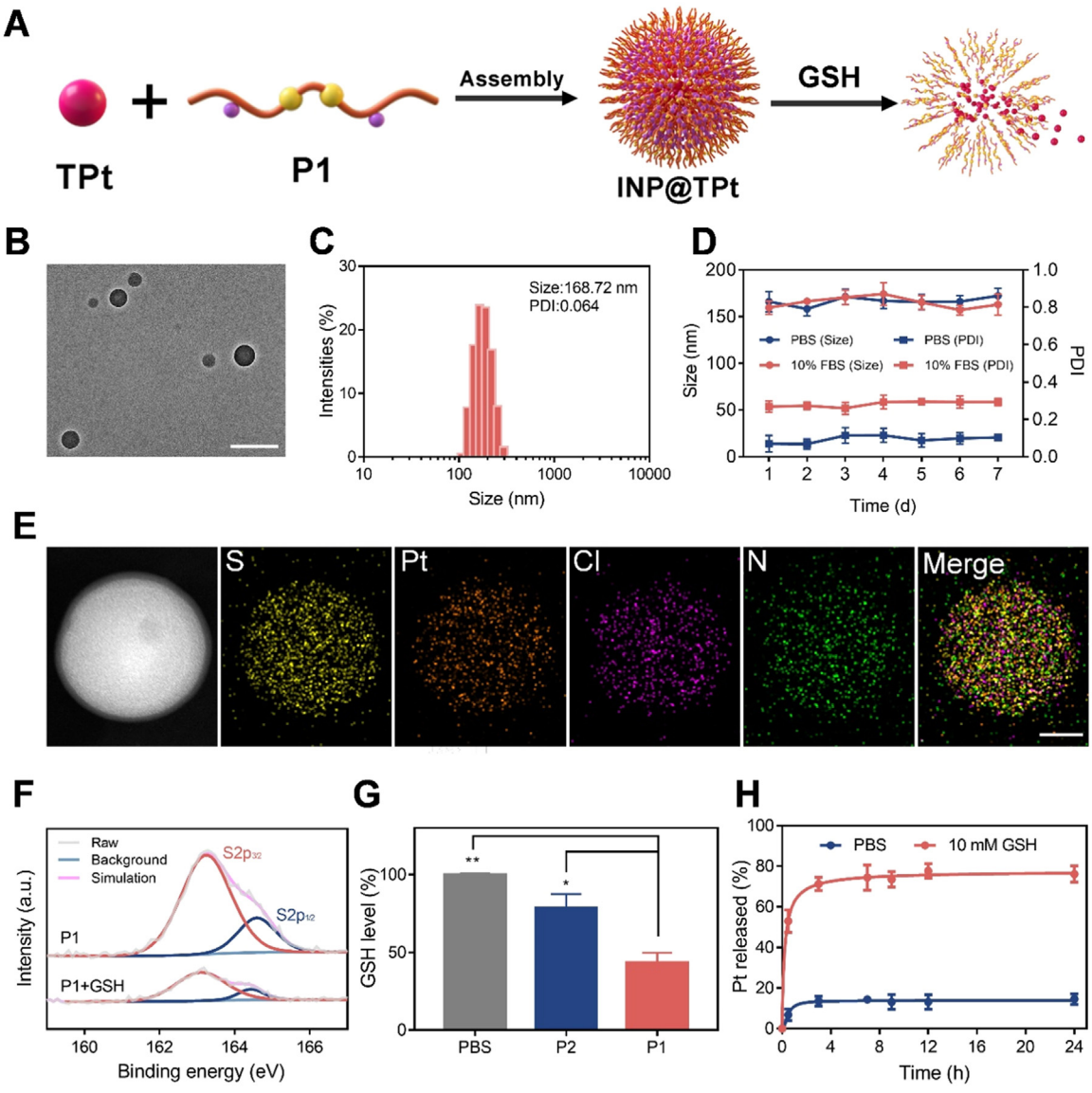

Fig. 1 – Characterization of INP@TPt. (A) Schematic illustration of INP@TPt preparation and GSH responsive NO and TPt release. (B) The SEM images and (C) hydrodynamic diameter of INP@TPt. Scale bar: 200 nm. (D) Hydrodynamic diameters and polydispersity index changes of INP@TPt upon incubating with 10% FBS or PBS for 7 d. (E) HAADF-STEM and EDS mapping images of INP@TPt. (F) XPS curves of S2p of P1 treated with or without GSH (10 mM) for 24 h. (G) GSH consumption of P1 and P2. (H) Pt release profiles of INP@TPt in the presence of 10 mM GSH and PBS. *P < 0.05, **P < 0.01.

decrease in intracellular GSH levels to approximately 71.90% after treatment with INP@TPt (Fig. 3A). This may have been due to degradation of P1, essentially involving GSH depletion. The triphenylphosphine group may have enabled TPt with a mitochondria-targeting ability. Subsequent experiments revealed that the Pt content of mitochondria was 4.32 ± 0.10 ng Pt/10^6 cells for the INP@TPt group, which was higher than CDDP (0.79 ± 0.16 ng Pt/10^6 cells) or INP@Pt(IV) (1.72 ± 0.32 ng Pt/10^6 cells) treatments (Fig. 3B). MMP collapse, a typical feature of mitochondrial damage, was also measured by JC-1 staining. A decreased red fluorescence (JC-1 aggregates) and increased green fluorescence (JC-1 monomers) usually indicate disrupted MMP. Fig. 3D showed that there was no increase in JC-1 monomers in the INP@Pt(IV) group (11.5%), when compared to the CDDP group (11.1%). In comparison, JC-1 monomers in mitochondria were significantly increased (55.8%) by INP@TPt, indicating MMP dissipation following INP@TPt treatment. Fig. 3C showed that INP@TPt decreased ATP production to 55.4%, possibly as a consequence of mitochondrial dysfunction, showing that INP@TPt overcame CDDP resistance because of robust GSH depletion and targeted mitochondria dysfunction.

3.4. *The gas treatment-based antitumor mechanism of INP@TPt in A2780DDP cells*

The nitrate ester group of ISMN contained in INP@TPt responds to intracellular GSH and produces NO [48,49]. The NO fluorescence probe (DAF-FM) was therefore used to assess NO levels in differently-treated A2780DDP cells, which

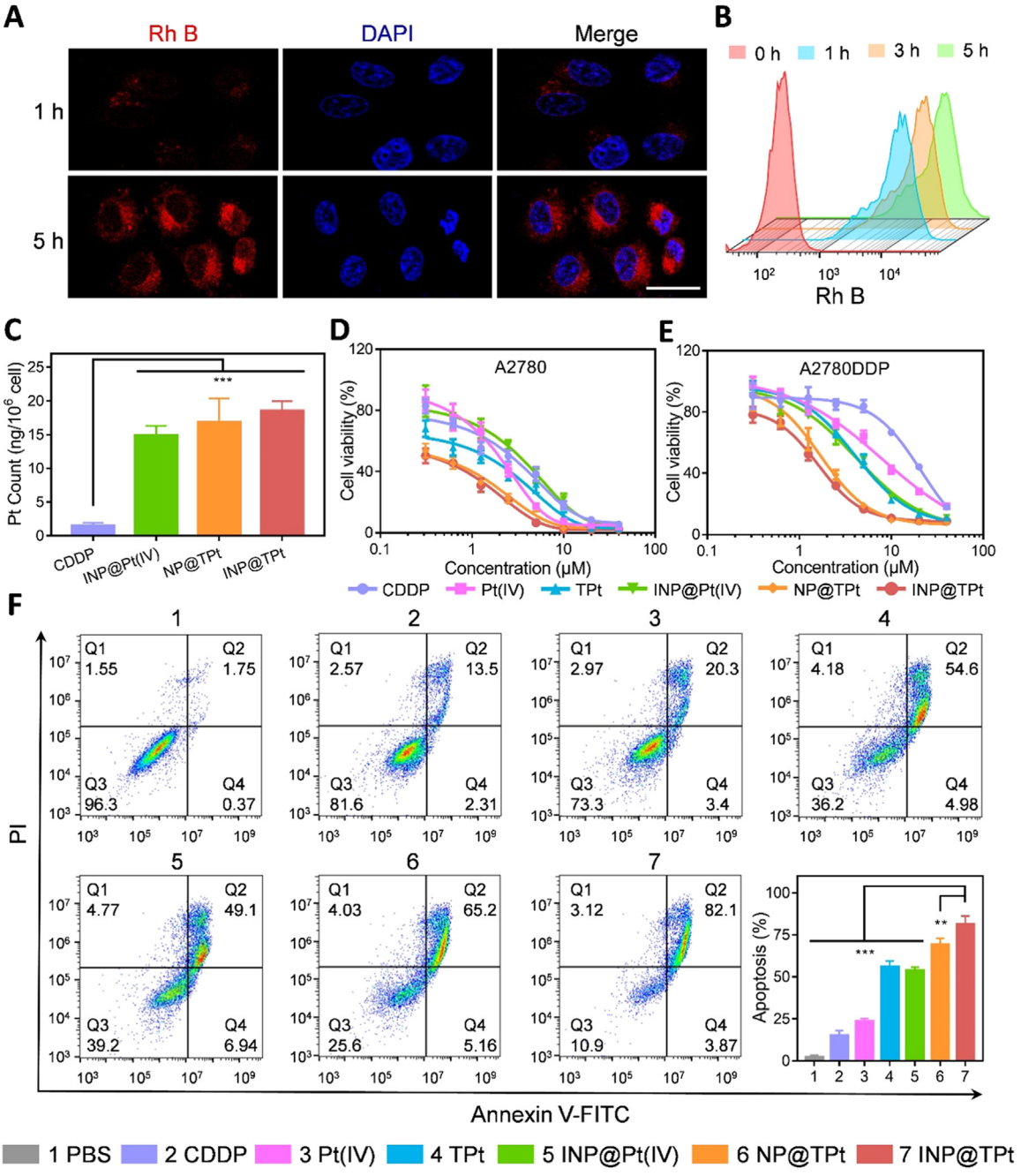

Fig. 2 – The endocytosis and cytotoxicity of INP@TPt. (A) Confocal scanning microscopy observation of INP@Rh B uptake by A2780DDP cells. Scale bar: 25 μm. (B) Time-dependent measurement of the intracellular level of INP@RhB in A2780DDP cells by flow cytometry. (C) The Pt count in A2780DDP cells after incubation with CDDP, INP@Pt(IV), NP@TPt, or INP@TPt at 37 °C. Viability curves of A2780 cells (D) and A2780DDP cells (E) after treatment with different concentrations of CDDP, Pt(IV), TPt, INP@Pt(IV), NP@TPt, INP@TPt for 48 h. (F) Apoptosis analysis of PBS, CDDP, Pt(IV), TPt, INP@Pt(IV), NP@TPt, or INP@TPt (3 μM Pt) on A2780DDP cells for 48 h. **P<0.05, ***P<0.001.

overexpressed GSH levels. Only after incubation of A2780DDP cells with INP@Pt(IV) and INP@TPt, was the strong green fluorescence of NO probe detected, which indicated efficient NO release in the intracellular reductive environment (Fig. 4A). FCM further showed similar results for NO production (Fig. 4C). When mitochondria were disrupted, abundant $O_2^{\bullet-}$ was released through the transfer of electrons to O_2 by the electron transport chain complex. The oxidation reaction between NO and $O_2^{\bullet-}$ would produce $ONOO^-$, which was a typical RNS with stronger lethality (Fig. 4B). The mitochondrial disruption-mediated production of $O_2^{\bullet-}$ was tested using a commercial fluorescent probe, 2,7-dichlorodihydrofluorescein diacetate (DCFH-DA). As shown in Fig. 4D, intracellular $O_2^{\bullet-}$ levels were significantly increased in TPt and NP@TPt

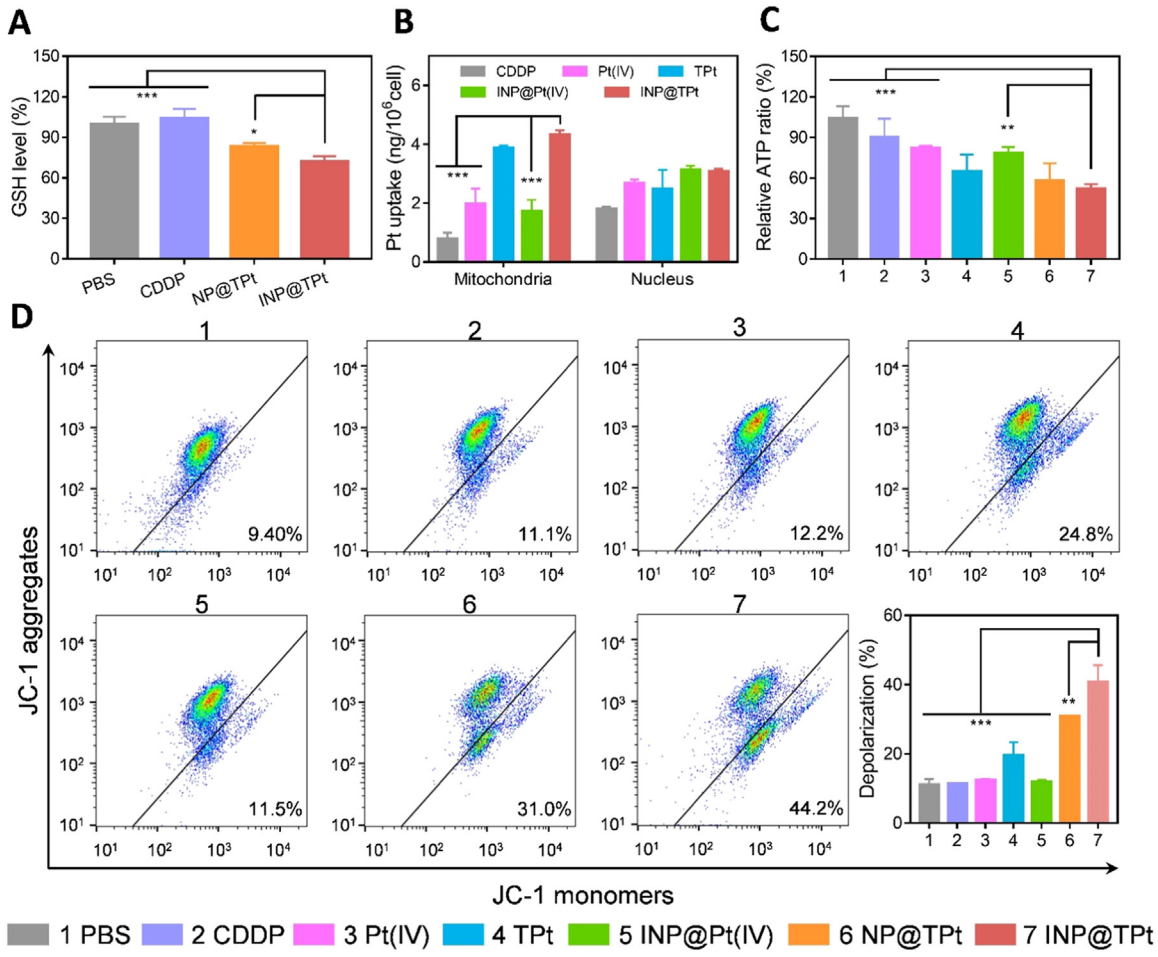

Fig. 3 – Analysis of GSH depletion and mitochondrial dysfunction. (A) Intracellular GSH level of A2780DDP cells treated with PBS, CDDP, NP@TPt, and INP@TPt (4 μM Pt). (B) Nucleus and mitochondrial distribution of Pt in A2780DDP cells after treatment with CDDP, Pt(IV), TPt, INP@Pt(IV), or INP@TPt (10 μM Pt) measured *via* inductively-coupled plasma mass spectrometry analysis. ATP decrease (C) and MMP depolarization (D) in A2780DDP cells treated with PBS, CDDP, Pt(IV), TPt, INP@Pt(IV), NP@TPt, or INP@TPt (3 μM Pt) for 48 h. *P<0.05, **P<0.01, ***P<0.001.

groups, except for the INP@TPt group, which was probably due to the reaction of $O_2^{\bullet-}$ with NO from INP@TPt to produce $ONOO^-$. In addition, almost no intracellular ROS was detected in the Pt(IV) and INP@Pt(IV) groups, which indirectly supported the effective disruption of mitochondria by TPt. Subsequently, a peroxynitrite assay kit (O52F) was used to measure the intracellular $ONOO^-$. As depicted in Fig. 4F, a strong green fluorescent signal of $ONOO^-$ can be observed in A2780DDP cells only after incubation with INP@TPt, indicating the simultaneous intracellular generation of NO and $O_2^{\bullet-}$. As expected, A2780DDP cells incubated with INP@Pt(IV) and TPt all failed to produce $ONOO^-$, due to the lack of either NO (TPt) or $O_2^{\bullet-}$ (INP@Pt(IV)) production. FCM further confirmed similar results for the production of $ONOO^-$ (Fig. 4E).

Western blotting was then used to elucidate the apoptotic pathway proteins of INP@TPt (Fig. 4G). INP@TPt-treated A2780DDP cells showed the highest expression of γ-H2A.X, further confirming the DNA strand breakage by $ONOO^-$ [50,51]. The expression of Bcl-2, an anti-apoptotic protein that was essential for the mitochondria-dependent apoptotic pathway, was lower in INP@TPt-treated cells [52]. Activated Caspase-3 (C-Caspase-3), one of the key "executors" of apoptosis *via* the mitochondria-dependent pathway, was upregulated following INP@TPt treatment [53–55]. C-Caspase-3 shears poly (ADP-ribase) polymerase (PARP) into two fragments, leading to apoptosis [56]. The results showed that expression of PARP was also down-regulated by INP@TPt. In summary, TPt released by INP@TPt disrupted mitochondria, thereby releasing $O_2^{\bullet-}$ and initiating the mitochondrial apoptosis pathway. In addition, NO produced by INP@TPt reacted with $O_2^{\bullet-}$ to produce $ONOO^-$ leading to DNA strand breakage. These two resulted in apoptosis together.

3.5. In vivo *antitumor effects and biocompatibility of INP@TPt*

In order to assess the *in vivo* antitumor effect and biocompatibility of INP@TPt, BALB/c nude mice were used to construct PDX^{OC} model, which can better recapitulate the microenvironmental and histological features of

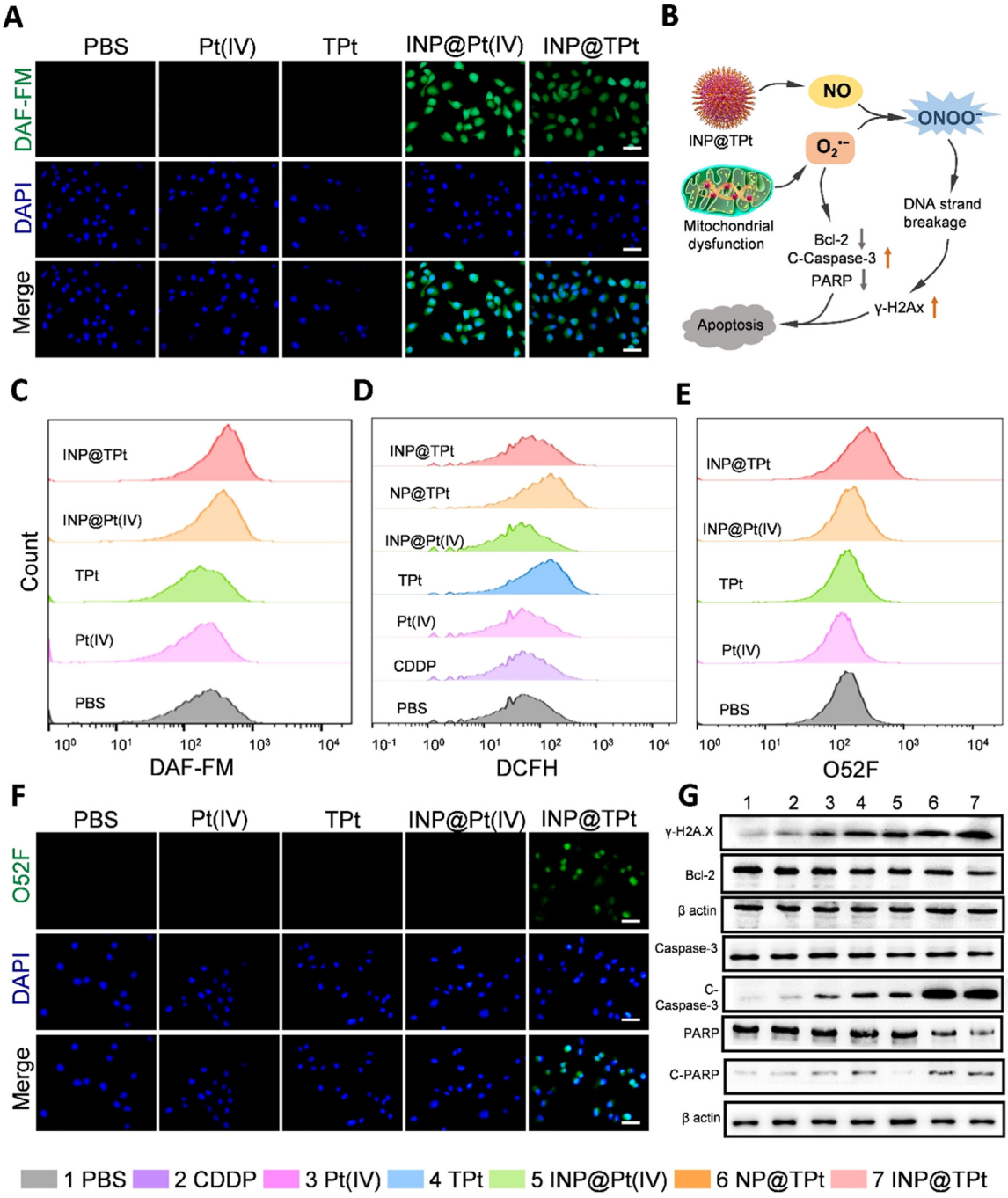

Fig. 4 – Production of NO, ROS, and RNS and the antitumor mechanism of INP@TPt in A2780DDP cells. CLSM (A) and quantitative analysis (C) by flow cytometry of intracellular NO production in A2780DDP cells after various treatments. Scale bar: 50 μm. (B) Illustration of antitumor mechanism of INP@TPt in drug resistance cells. (D) ROS generation in A2780DDP cells after multiple treatments. Quantitative analysis (E) for flow cytometry and CLSM images (F) of intracellular RNS generation in A2780DDP cells after multiple treatments. (G) Western blot of γ-H2A.X, Bcl-2, Caspase 3, C-Caspase-3, PARP, C-PARP, β-actin expression of A2780DDP cells after treating with different formulations.

primary tumors [57,58]. (Fig. 5A). The biodistribution of Cy5.5-labeled INP@Cy5.5 was monitored in the PDX^{OC} model using an *in vivo* fluorescence-imaging system (IVIS). After 24 h postinjection *via* the tail vein, *in vivo* and *ex vivo* fluorescence significantly accumulated within tumors, facilitating subsequent treatment at the tumor site (Fig. 5B and S15). Semi-quantitative analysis of fluorescence intensities showed that the fluorescence intensity was significantly stronger in tumor tissue than in major organs (Fig. 5C). When the tumor reached a volume of 50–100 mm^3, the mice were randomly divided into five groups and injected intravenously with either PBS, CDDP, INP@Pt(IV), NP@TPt, or

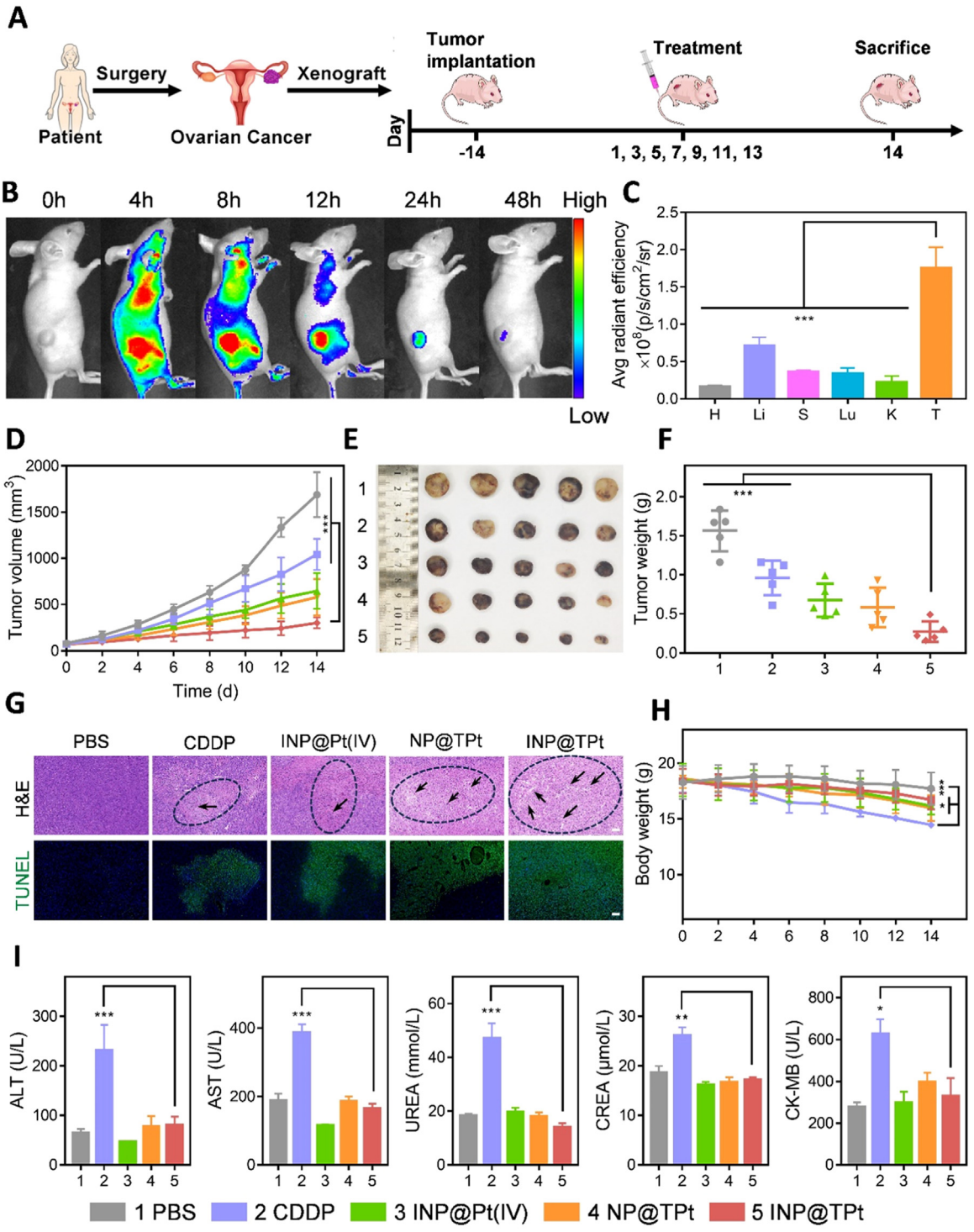

Fig. 5 – Therapeutic efficacy of INP@TPt using the PDX^{OC} model. (A) Schematic illustration of therapeutic regimen on ovarian cancer PDX model. (B) *In vivo* fluorescence distribution of INP@Cy5.5 in PDX^{OC} model. (C) The semi-quantitative analysis of the fluorescence intensity of tumors and major organs of mice intravenously injected with INP@Cy5.5, after 24 h. (D) Tumor growth curves of mice receiving different treatments. Photograph (E) and weight (F) of tumors isolated from mice after different treatments on day 14. (G) Hematoxylin & eosin (H&E) and TUNEL staining images in tumors isolated from mice with different treatments. Scale bar: 100 μm. Oval: Apoptotic area. Arrows: Apoptosis markers, including nuclear condensation and apoptotic body formation. (H) Body weight changes of mice after different treatments. (I) Serum biochemical analysis of PDX^{OC} model after treatment on day 14. ALT, alanine transaminase. AST, aspartate aminotransferase. UREA, urea. CREA, creatinine. CK-MB, creatine kinase-MB. *P<0.05, **P<0.01, ***P<0.001.

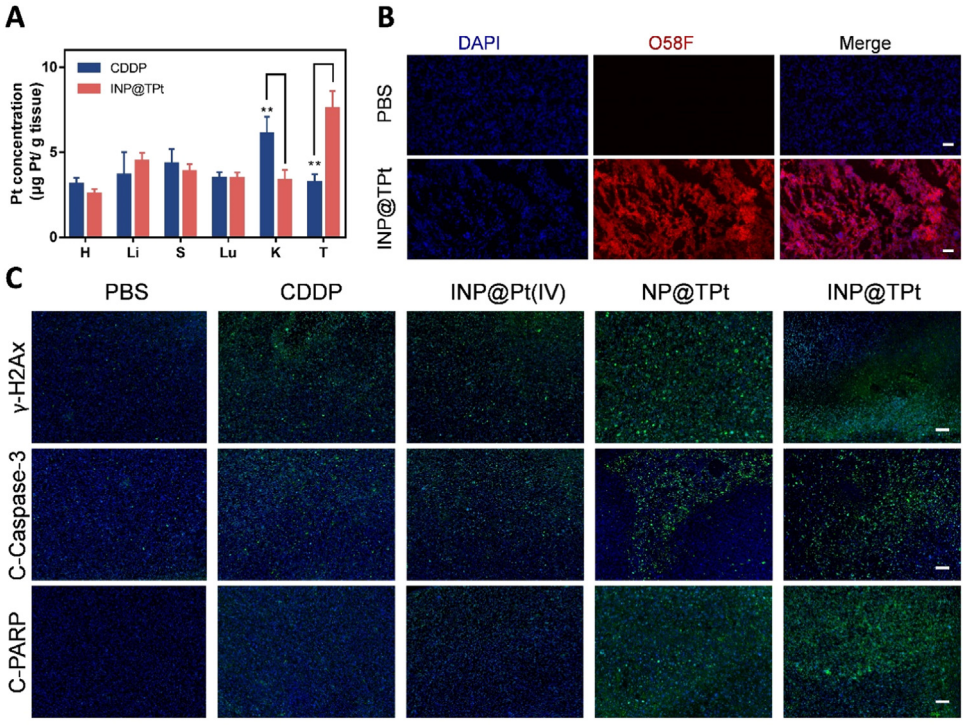

Fig. 6 – *In vivo* antitumor mechanism of INP@TPt. (A) Biodistributions of Pt in tumors and major organs at 24 h post-administration. (B) $ONOO^-$ analysis of tumors. Scale bar: 50 μm. (C) γ-H2A.X, C-Caspase-3, and C-PARP immunofluorescence staining of tumor sections. Scale bar: 100 μm. **$P<0.01$.

INP@TPt (1.5 mg/kg Pt) every 2 d Tumor volume in the PBS group increased rapidly to 1679 mm^3, whereas the tumor volume of INP@TPt group was smaller, when compared to the CDDP group (302 mm^3 *vs* 1042 mm^3) (Fig. 5D-5E). In addition, Fig. 5F showed that mice treated with INP@TPt had the smallest tumor weight (0.27 ± 0.12 g), when compared to those treated with PBS (1.57 ± 0.23 g) and CDDP (0.96 ± 0.20 g). The results of hematoxylin-eosin (H&E) staining and terminal deoxynucleotidyl transferase dUTP nick-end labeling (TUNEL) analyses further confirmed the superior antitumor effect of INP@TPt (Fig. 5G). As shown in Fig. 5H, there were no significant fluctuation in the body weight of mice during treatment, except for weight loss observed in the CDDP group due to serious systemic toxicity. In addition, all treated groups were assessed for various blood biochemical parameters (ALT, AST, UREA, CREA, and CK-MB) and showed negligible systemic toxicity compared to the PBS group, except that the CDDP treated group exhibited significant systemic toxicity (Fig. 5I). H&E staining of the major organs for histopathological changes also indicated that INP@TPt induced less systemic toxicity throughout the treatment, demonstrating excellent biocompatibility (Fig. S16).

3.6. In vivo *antitumor mechanism of INP@TPt*

ICP-MS was used to estimate Pt concentration to further identify the biodistribution of INP@TPt. The results showed that Pt concentration in the tumor was significantly higher in INP@TPt (7.58 ± 0.84 μg Pt/g tissue) than in the CDDP group (3.22 ± 0.16 μg Pt/g tissue) (Fig. 6A), suggesting a good tumor-specific accumulation of INP@TPt due to the EPR effect, facilitating the treatment of tumor-specific sites. In addition, GSH levels was measured in INP@TPt-treated tumors after 48 h of intravenous injections, which showed that the GSH level in the INP@TPt group decreased about 3-fold, when compared to the PBS group, demonstrating its GSH depletion capability (Fig. S17). The production and action of $ONOO^-$ in tumor tissues were further investigated by the peroxynitrite frozen section staining kit. A high intra-tumor $ONOO^-$ level was observed in INP@TPt-treated mice, as shown by the stronger red fluorescence, which was attributable to the simultaneous release of $O_2^{\bullet-}$ and NO in the tumor tissue (Fig. 6B). The significant increase in the DNA damage indicator (γ-H2A.X), and the mitochondrial apoptotic pathway indicators (C-Caspase-3, C-PARP) confirmed the mechanism of antitumor effect *in vivo* in INP@TPt (Fig. 6C).

4. Conclusion

In conclusion, we have developed a nanocomposite INP@TPt assembled from mitochondrial-targeted cisplatin and NO donor contained amphiphile. In contrast to conventional cisplatin, INP@TPt had an enhanced uptake in drug resistance tumor cells bexause it did not rely on a CTR1-dependent transporting process. After reaction with excessive GSH in tumor cells, NO and mitochondrial-targeted cisplatin were released. The dysfunction of mitochondrial induced production of $O_2^{\bullet-}$, further reacted with NO to generate highly toxic $ONOO^-$. Due to the synergistic effects against

the cascade drug resistance mechanism, the INP@TPt showed significant inhibition of tumor growth *in vivo* and significantly decreased the side-effect of free CDDP, using the PDX^{OC} mouse model. Overall, our systematic strategy demonstrates considerable potential in overcoming platinum CDR, providing practical applications in anticancer therapy.

Conflicts of interest

The authors report no conflicts of interest. The authors alone are responsible for the content and writing of this article.

Acknowledgements

We extend heartfelt gratitude to Professor Haihua Xiao and his research team for generously providing the human ovarian cancer patient-derived tumor xenograft (PDX^{OC}) model for our study. Their invaluable support has played an important role in our research journey. This work was supported by the Guangdong Basic and Applied Basic Research Foundation of China (No. 2021A1515011050) and President Foundation of The Third Affiliated Hospital of Southern Medical University [grant number YM202202].

Supplementary materials

The characterizations, synthesis, drug release studies, cellular uptake, animal models and *in vitro* antitumor efficacy can be found in the Supporting Information.

Supplementary material associated with this article can be found, in the online version, at doi:10.1016/j.ajps.2023.100872.

References

[1] Siegel RL, Miller KD, Jemal A. Cancer statistics. CA Cancer J Clin 2020;70:7–30 2020.
[2] Hanker LC, Loibl S, Burchardi N, Pfisterer J, Meier W, Pujade-Lauraine E, et al. The impact of second to sixth line therapy on survival of relapsed ovarian cancer after primary taxane/platinum-based therapy. Ann Oncol 2012;23:2605–12.
[3] Moufarrij S, Dandapani M, Arthofer E, Gomez S, Srivastava A, Lopez-Acevedo M, et al. Epigenetic therapy for ovarian cancer: promise and progress. Clin Epigenetics 2019;11:7.
[4] Blagden SP, Nicum S. A source of hope for platinum-resistant ovarian cancer? Lancet 2021;397:254–6.
[5] Chan JK, Chow S, Bhowmik S, Mann A, Kapp DS, Coleman RL. Metastatic gynecologic malignancies: advances in treatment and management. Clin Exp Metastas 2018;35:521–33.
[6] Muñoz-Galván S, Felipe-Abrio B, Verdugo-Sivianes EM, Perez M, Jiménez-García MP, Suarez-Martinez E, et al. Downregulation of MYPT1 increases tumor resistance in ovarian cancer by targeting the Hippo pathway and increasing the stemness. Mol Cancer 2020;19:7.
[7] Xie P, Wang Y, Wei D, Zhang L, Zhang B, Xiao H, et al. Nanoparticle-based drug delivery systems with platinum drugs for overcoming cancer drug resistance. J Mater Chem B 2021;9:5173–94.
[8] Wang L, Yu Y, Wei D, Zhang L, Zhang X, Zhang G, et al. A systematic strategy of combinational blow for overcoming cascade drug resistance *via* NIR-light-triggered hyperthermia. Adv Mater 2021:2100599.
[9] Blair BG, Larson CA, Safaei R, Howell SB. Copper transporter 2 regulates the cellular accumulation and cytotoxicity of cisplatin and carboplatin. Clin Cancer Res 2009;15:4312–21.
[10] öhrvik H, Thiele DJ. The role of Ctr1 and Ctr2 in mammalian copper homeostasis and platinum-based chemotherapy. J Trace Elem Med Bio 2015;31:178–82.
[11] Ling M, Sun R, Li G, Syeda MZ, Ma W, Mai Z, et al. NIR-II emissive dye based polymer nanoparticle targeting EGFR for oral cancer theranostics. Nano Res 2022;15:6288–96.
[12] Sun R, Ma W, Ling M, Tang C, Zhong M, Dai J, et al. pH-activated nanoplatform for visualized photodynamic and ferroptosis synergistic therapy of tumors. J Control Release 2022;350:525–37.
[13] Choudhary D, Goykar H, Karanwad T, Kannaujia S, Gadekar V, Misra M. An understanding of mitochondria and its role in targeting nanocarriers for diagnosis and treatment of cancer. Asian J Pharm Sci 2021;16(4):397–418.
[14] Goto S, Iida T, Cho S, Oka M, Kohno S, Kondo T. Overexpression of glutathione S-transferase pi enhances the adduct formation of cisplatin with glutathione in human cancer cells. Free Radic Res 1999;31:549–58.
[15] Kasherman Y, Sturup S, Gibson D. Is glutathione the major cellular target of cisplatin? A study of the interactions of cisplatin with cancer cell extracts. J Med Chem 2009;52:4319–28.
[16] Yang Y, Sun B, Zuo S, Li X, Zhou S, Li L, et al. Trisulfide bond-mediated doxorubicin dimeric prodrug nanoassemblies with high drug loading, high self-assembly stability, and high tumor selectivity. Sci Adv 2020;6:eabc1725.
[17] Zuo S, Sun B, Yang Y, Zhou S, Zhang Y, Guo M, et al. Probing the superiority of diselenium bond on docetaxel dimeric prodrug nanoassemblies: small roles taking big responsibilities. Small 2020;16:e2005039.
[18] Duan M, Ulibarri J, Liu KJ, Mao P. Role of nucleotide excision repair in cisplatin resistance. Int J Mol Sci 2020;21:9248.
[19] Jackson SP, Bartek J. The DNA-damage response in human biology and disease. Nature 2009;461:1071–8.
[20] Li Y, Luo K, Yin Y, Wu C, Deng M, Li L, et al. USP13 regulates the RAP80-BRCA1 complex dependent DNA damage response. Nat Commun 2017;8:15752.
[21] Smiraglia DJ, Kulawiec M, Bistulfi GL, Gupta SG, Singh KK. A novel role for mitochondria in regulating epigenetic modification in the nucleus. Cancer Biol Ther 2008;7:1182–90.
[22] Wang K, Zhu C, He Y, Zhang Z, Zhou W, Muhammad N, et al. Restraining cancer cells by dual metabolic inhibition with a mitochondrion-targeted platinum (II) complex. Angew Chem Int Ed Engl 2019;58:4638–43.
[23] Zhang W, Hu X, Shen Q, Xing D. Mitochondria-specific drug release and reactive oxygen species burst induced by polyprodrug nanoreactors can enhance chemotherapy. Nat Commun 2019;10:1704.
[24] Gong N, Ma X, Ye X, Zhou Q, Chen X, Tan X, et al. Carbon-dot-supported atomically dispersed gold as a mitochondrial oxidative stress amplifier for cancer treatment. Nat Nanotechnol 2019;14:379–87.
[25] Zheng P, Ding J. Calcium ion nanomodulators for mitochondria-targeted multimodal cancer therapy. Asian J Pharm Sci 2022;17(1):1–3.
[26] Zheng P, Ding B, Shi R, Jiang Z, Xu W, Li G, et al. A multichannel Ca^{2+} nanomodulator for multilevel mitochondrial destruction-dediated cancer therapy. Adv Mater 2021;33:e2007426.
[27] Addabbo F, Montagnani M, Goligorsky MS. Mitochondria and reactive oxygen species. Hypertension 2009;53:885–92.

[28] Circu ML, Aw TY. Reactive oxygen species, cellular redox systems, and apoptosis. Free Radic Biol Med 2010;48:749–62.
[29] Liu P, Wang Y, Liu Y, Tan F, Li J, Li N. S-nitrosothiols loaded mini-sized Au@silica nanorod elicits collagen depletion and mitochondrial damage in solid tumor treatment. Theranostics 2020;10:6774–89.
[30] Nathan C, Ding A. Snapshot: reactive oxygen intermediates (ROI). Cell 2010;140:951.
[31] Qi J, Xiong Y, Cheng K, Huang Q, Cao J, He F, Mei L, Liu G, Deng W. Heterobifunctional PEG-grafted black phosphorus quantum dots: "Three-in-One" nano-platforms for mitochondria-targeted photothermal cancer therapy. Asian J Pharm Sci 2021;16(2):222–35.
[32] Roger AJ, Muñoz-Gómez SA, Kamikawa R. The origin and diversification of mitochondria. Curr Biol 2017;27:R1177–92.
[33] Turrens JF. Mitochondrial formation of reactive oxygen species. J Physiol 2003;552:335–44.
[34] Zorov DB, Juhaszova M, Sollott SJ. Mitochondrial reactive oxygen species (ROS) and ROS-induced ROS release. Physiol Rev 2014;94:909–50.
[35] Calcerrada P, Peluffo G, Radi R. Nitric oxide-derived oxidants with a focus on peroxynitrite: molecular targets, cellular responses and therapeutic implications. Curr Pharm Des 2011;17:3905–32.
[36] Moldogazieva NT, Lutsenko SV, Terentiev AA. Reactive oxygen and nitrogen species-induced protein modifications: implication in carcinogenesis and anticancer therapy. Cancer Res 2018;78:6040–7.
[37] Fu S, Liang S, Jiang D, Yang R, Zhang Z, Chang L, Zhang X, Liu Y, Zhang N. Gas-blasting nanocapsules to accelerate carboplatin lysosome release and nucleus delivery for prostate cancer treatment. Asian J Pharm Sci 2021;16(2):192–202.
[38] Weidinger A, Kozlov AV. Biological activities of reactive oxygen and nitrogen species: oxidative stress *versus* signal transduction. Biomolecules 2015;5:472–84.
[39] Radi R, Beckman JS, Bush KM, Freeman BA. Peroxynitrite-induced membrane lipid peroxidation: the cytotoxic potential of superoxide and nitric oxide. Arch Biochem Biophys 1991;288:481–7.
[40] Virág L, SzabóE Gergely P, Szabó C. Peroxynitrite-induced cytotoxicity: mechanism and opportunities for intervention. Toxicol Lett 2003;140-141:113–24.
[41] Wang Z, Zhan M, Li W, Chu C, Xing D, Lu S, et al. Photoacoustic cavitation-ignited reactive oxygen species to amplify peroxynitrite burst by photosensitization-free polymeric nanocapsules. Angew Chem Int Ed Engl 2021;60:4720–31.
[42] Beckman JS, Beckman TW, Chen J, Marshall PA, Freeman BA. Apparent hydroxyl radical production by peroxynitrite: implications for endothelial injury from nitric oxide and superoxide. Proc Natl Acad Sci USA 1990;87:1620–4.
[43] Du Z, Zhang X, Guo Z, Xie J, Dong X, Zhu S, et al. X-Ray-controlled generation of peroxynitrite based on nanosized LiLuF(4):Ce^{3+} scintillators and their applications for radiosensitization. Adv Mater 2018;30:e1804046.
[44] Ferrer-Sueta G, Campolo N, Trujillo M, Bartesaghi S, Carballal S, Romero N, et al. Biochemistry of peroxynitrite and protein tyrosine nitration. Chem Rev 2018;118:1338–408.
[45] Pacher P, Beckman JS, Liaudet L. Nitric oxide and peroxynitrite in health and disease. Physiol Rev 2007;87:315–424.
[46] SzabóC Ischiropoulos H, Radi R. Peroxynitrite: biochemistry, pathophysiology and development of therapeutics. Nat Rev Drug Discov 2007;6:662–80.
[47] Ma Z, Hu P, Guo C, Wang D, Zhang X, Chen M, et al. Folate-mediated and pH-responsive chidamide-bound micelles encapsulating photosensitizers for tumor-targeting photodynamic therapy. Int J Nanomedicine 2019;14:5527–40.
[48] Chiesa JJ, Baidanoff FM, Golombek DA. Don't just say no: differential pathways and pharmacological responses to diverse nitric oxide donors. Biochem Pharmacol 2018;156:1–09.
[49] Wang PG, Xian M, Tang X, Wu X, Wen Z, Cai T, et al. Nitric oxide donors: chemical activities and biological applications. Chem Rev 2002;102:1091–134.
[50] Holme JA, Nyvold HE, Tat V, Arlt VM, Bhargava A, Gutzkow KB, et al. Mechanisms linked to differences in the mutagenic potential of 1,3-dinitropyrene and 1,8-dinitropyrene. Toxicol Rep 2014;1:459–73.
[51] Vadivel GS, Bonczek O, Wang L, Chen S, Fahraeus R. p53 mRNA metabolism links with the DNA damage response. Genes 2021;12:1446.
[52] Chipuk JE, Kuwana T, Bouchier-Hayes L, Droin NM, Newmeyer DD, Schuler M, et al. Direct activation of Bax by p53 mediates mitochondrial membrane permeabilization and apoptosis. Science 2004;303:1010–14.
[53] Cohen GM. Caspases: the executioners of apoptosis. Biochem J 1997;326(Pt 1):1–16.
[54] Krajewska M, Wang HG, Krajewski S, Zapata JM, Shabaik A, Gascoyne R, et al. Immunohistochemical analysis of *in vivo* patterns of expression of CPP32 (Caspase-3), a cell death protease. Cancer Res 1997;57:1605–13.
[55] Xing L, Lyu JY, Yang Y, Cui PF, Gu LQ, Qiao JB, et al. pH-Responsive de-PEGylated nanoparticles based on triphenylphosphine-quercetin self-assemblies for mitochondria-targeted cancer therapy. Chem Commun 2017;53:8790–3.
[56] Posmantur R, Wang KK, Nath R, Gilbertsen RB. A purine nucleoside phosphorylase (PNP) inhibitor induces apoptosis via caspase-3-like protease activity in MOLT-4 T cells. Immunopharmacology 1997;37:231–44.
[57] Yang Y, Yu Y, Chen H, Meng X, Ma W, Yu M, et al. Illuminating platinum transportation while maximizing therapeutic efficacy by gold nanoclusters via simultaneous near-infrared-I/II imaging and glutathione scavenging. ACS Nano 2020;14:13536–47.
[58] Zhang J, Zhao B, Chen S, Wang Y, Zhang Y, Wang Y, et al. Near-infrared light irradiation induced mild hyperthermia enhances glutathione depletion and DNA interstrand cross-link formation for efficient chemotherapy. ACS Nano 2020;14:14831–45.